Enhanced detection limit by dark mode perturbation in 2D photonic crystal slab refractive index sensors

Costa Nicolaou,[1,2,4] Wah Tung Lau,[3,4] Raanan Gad,[1,2,4] Hooman Akhavan,[1,2,4] Ryan Schilling,[1,2] and Ofer Levi[1,2*]

[1]*The Edward S. Rogers Sr. Department of Electrical and Computer Engineering, University of Toronto, 10 King's College Road, Toronto, ON M5S 3G4, Canada*

[2]*Institute of Biomaterials and Biomedical Engineering, University of Toronto,164 College Street, Toronto, ON M5S 3G9, Canada*

[3]*Department of Physics, 60 St. George Street, University of Toronto, Toronto, ON M5S 1A7, Canada*

[4]*These authors contributed equally to this work.*

**ofer.levi@utoronto.ca*

Abstract: We demonstrate for the first time a 300nm thick, 300μm × 300μm 2D dielectric photonic crystal slab membrane with a quality factor of 10,600 by coupling light to slightly perturbed dark modes through alternating nano-hole sizes. The newly created fundamental guided resonances greatly reduce nano-fabrication accuracy requirements. Moreover, we created a new layer architecture resulting in electric field enhancement at the interface between the slab and sensing regions, and spectral sensitivity of >800 nm/RIU, that is, >0.8 of the single-mode theoretical upper limit of spectral sensitivity.

OCIS codes: (350.4238) Nanophotonics and photonic crystals; (280.1415) Biological sensing and sensors; (050.6624) Subwavelength structures; (260.5740) Resonance; (170.0170) Medical optics and biotechnology; (220.4241) Nanostructure fabrication.

References and links

1. I. M. White and X. Fan, "On the performance quantification of resonant refractive index sensors," Opt. Express **16**(2), 1020–1028 (2008).
2. F. Vollmer and L. Yang, "Review Label-free detection with high-Q microcavities: a review of biosensing mechanisms for integrated devices," Nanophoton. **1**(3–4), 267–291 (2012).
3. X. Fan, I. M. White, S. I. Shopova, H. Zhu, J. D. Suter, and Y. Sun, "Sensitive optical biosensors for unlabeled targets: A review," Anal. Chim. Acta **620**(1), 8–26 (2008).
4. P. S. Cremer, "Label-free detection becomes crystal clear," Nat. Biotechnol. **22**(2), 172–173 (2004).
5. B. R. Schudel, C. J. Choi, B. T. Cunningham, and P. J. Kenis, "Microfluidic chip for combinatorial mixing and screening of assays," Lab Chip **9**(12), 1676–1680 (2009).
6. P. Y. Li, B. Lin, J. Gerstenmaier, and B. T. Cunningham, "A new method for label-free imaging of biomolecular interactions," Sens. Actuators B Chem. **99**(1), 6–13 (2004).
7. A. Serpengüzel, S. Arnold, and G. Griffel, "Excitation of resonances of microspheres on an optical fiber," Opt. Lett. **20**(7), 654–656 (1995).
8. A. M. Armani, R. P. Kulkarni, S. E. Fraser, R. C. Flagan, and K. J. Vahala, "Label-free, single-molecule detection with optical microcavities," Science **317**(5839), 783–787 (2007).
9. L. L. Chan, S. L. Gosangari, K. L. Watkin, and B. T. Cunningham, "Label-free imaging of cancer cells using photonic crystal biosensors and application to cytotoxicity screening of a natural compound library," Sens. Actuators B Chem. **132**(2), 418–425 (2008).
10. J. T. Robinson, L. Chen, and M. Lipson, "On-chip gas detection in silicon optical microcavities," Opt. Express **16**(6), 4296–4301 (2008).
11. W.-C. Lai, S. Chakravarty, Y. Zou, and R. T. Chen, "Silicon nano-membrane based photonic crystal microcavities for high sensitivity bio-sensing," Opt. Lett. **37**(7), 1208–1210 (2012).
12. S. Soria, S. Berneschi, M. Brenci, F. Cosi, G. Nunzi Conti, S. Pelli, and G. C. Righini, "Optical microspherical resonators for biomedical sensing," Sensors **11**(1), 785–805 (2011).
13. P. R. Villeneuve, S. Fan, and J. D. Joannopoulos, "Microcavities in photonic crystals: Mode symmetry, tunability, and coupling efficiency," Phys. Rev. B Condens. Matter **54**(11), 7837–7842 (1996).

#197981 - $15.00 USD Received 19 Sep 2013; revised 29 Nov 2013; accepted 4 Dec 2013; published 13 Dec 2013

14. D. Shankaran, K. Gobi, and N. Miura, "Recent advancements in surface plasmon resonance immunosensors for detection of small molecules of biomedical, food and environmental interest," Sens. Actuators B Chem. **121**(1), 158–177 (2007).
15. J. Homola, "Present and future of surface plasmon resonance biosensors," Anal. Bioanal. Chem. **377**(3), 528–539 (2003).
16. S. McCall, A. Levi, R. Slusher, S. Pearton, and R. Logan, "Whispering-gallery mode microdisk lasers," Appl. Phys. Lett. **60**(3), 289–291 (1992).
17. V. Sandoghdar, F. Treussart, J. Hare, V. Lefèvre-Seguin, J. Raimond, and S. Haroche, "Very low threshold whispering-gallery-mode microsphere laser," Phys. Rev. A **54**(3), R1777–R1780 (1996).
18. V. Lefèvre-Seguin and S. Haroche, "Towards cavity-QED experiments with silica microspheres," Mater. Sci. Eng. B **48**(1), 53–58 (1997).
19. D. Vernooy, A. Furusawa, N. P. Georgiades, V. Ilchenko, and H. Kimble, "Cavity QED with high-Q whispering gallery modes," Phys. Rev. A **57**(4), 2293–2296 (1998).
20. A. Yariv, Y. Xu, R. K. Lee, and A. Scherer, "Coupled-resonator optical waveguide: a proposal and analysis," Opt. Lett. **24**(11), 711–713 (1999).
21. F. Treussart, V. Ilchenko, J.-F. Roch, J. Hare, V. Lefevre-Seguin, J.-M. Raimond, and S. Haroche, "Evidence for intrinsic Kerr bistability of high-Q microsphere resonators in superfluid helium," Eur. Phys. J. D **1**(3), 235 (1998).
22. S. M. Spillane, T. J. Kippenberg, and K. J. Vahala, "Ultralow-threshold Raman laser using a spherical dielectric microcavity," Nature **415**(6872), 621–623 (2002).
23. S. Lin, W. Zhu, Y. Jin, and K. B. Crozier, "Surface-enhanced Raman scattering with Ag nanoparticles optically trapped by a photonic crystal cavity," Nano Lett. **13**(2), 559–563 (2013).
24. E. Jaquay, L. J. Martínez, C. A. Mejia, and M. L. Povinelli, "Light-assisted, templated self-assembly using a photonic-crystal slab," Nano Lett. **13**(5), 2290–2294 (2013).
25. M. Righini, P. Ghenuche, S. Cherukulappurath, V. Myroshnychenko, F. J. García de Abajo, and R. Quidant, "Nano-optical trapping of Rayleigh particles and Escherichia coli bacteria with resonant optical antennas," Nano Lett. **9**(10), 3387–3391 (2009).
26. S. Fan and J. Joannopoulos, "Analysis of guided resonances in photonic crystal slabs," Phys. Rev. B **65**(23), 235112 (2002).
27. T. Ochiai and K. Sakoda, "Dispersion relation and optical transmittance of a hexagonal photonic crystal slab," Phys. Rev. B **63**(12), 125107 (2001).
28. M. El Beheiry, V. Liu, S. Fan, and O. Levi, "Sensitivity enhancement in photonic crystal slab biosensors," Opt. Express **18**(22), 22702–22714 (2010).
29. J. D. Joannopoulos, S. G. Johnson, J. N. Winn, and R. D. Meade, Photonic crystals: molding the flow of light (Princeton university press, 2011).
30. V. Liu, M. Povinelli, and S. Fan, "Resonance-enhanced optical forces between coupled photonic crystal slabs," Opt. Express **17**(24), 21897–21909 (2009).
31. O. Kilic, M. Digonnet, G. Kino, and O. Solgaard, "Controlling uncoupled resonances in photonic crystals through breaking the mirror symmetry," Opt. Express **16**(17), 13090–13103 (2008).
32. R. Wang, X.-H. Wang, B.-Y. Gu, and G.-Z. Yang, "Effects of shapes and orientations of scatterers and lattice symmetries on the photonic band gap in two-dimensional photonic crystals," J. Appl. Phys. **90**(9), 4307 (2001).
33. W. M. Robertson, G. Arjavalingam, R. D. Meade, K. D. Brommer, A. M. Rappe, and J. D. Joannopoulos, "Measurement of photonic band structure in a two-dimensional periodic dielectric array," Phys. Rev. Lett. **68**(13), 2023–2026 (1992).
34. W. M. Robertson, G. Arjavalingam, R. D. Meade, K. D. Brommer, A. M. Rappe, and J. D. Joannopoulos, "Measurement of the photon dispersion relation in two-dimensional ordered dielectric arrays," J. Opt. Soc. Am. B **10**(2), 322 (1993).
35. K. Sakoda, "Symmetry, degeneracy, and uncoupled modes in two-dimensional photonic lattices," Phys. Rev. B Condens. Matter **52**(11), 7982–7986 (1995).
36. J. Lee, B. Zhen, S.-L. Chua, W. Qiu, J. D. Joannopoulos, M. Soljačić, and O. Shapira, "Observation and differentiation of unique high-Q optical resonances near zero wave vector in macroscopic photonic crystal slabs," Phys. Rev. Lett. **109**(6), 067401 (2012).
37. F. Lemarchand, A. Sentenac, and H. Giovannini, "Increasing the angular tolerance of resonant grating filters with doubly periodic structures," Opt. Lett. **23**(15), 1149–1151 (1998).
38. A.-L. Fehrembach, A. Talneau, O. Boyko, F. Lemarchand, and A. Sentenac, "Experimental demonstration of a narrowband, angular tolerant, polarization independent, doubly periodic resonant grating filter," Opt. Lett. **32**(15), 2269–2271 (2007).
39. N.-V.-Q. Tran, S. Combrié, and A. De Rossi, "Directive emission from high-Q photonic crystal cavities through band folding," Phys. Rev. B **79**(4), 041101 (2009).
40. A. Yariv and P. Yeh, Photonics: Optical Electronics in Modern Communications (The Oxford Series in Electrical and Computer Engineering) (Oxford University Press, Inc., 2006).
41. V. Liu and S. Fan, "S4: A free electromagnetic solver for layered periodic structures," Comput. Phys. Commun. **183**(10), 2233–2244 (2012).
42. Z. Yu and S. Fan, "Extraordinarily high spectral sensitivity in refractive index sensors using multiple optical modes," Opt. Express **19**(11), 10029–10040 (2011).

#197981 - $15.00 USD Received 19 Sep 2013; revised 29 Nov 2013; accepted 4 Dec 2013; published 13 Dec 2013

43. O. Levi, M. M. Lee, J. Zhang, V. Lousse, S. R. Brueck, S. Fan, and J. S. Harris, "Sensitivity analysis of a photonic crystal structure for index-of-refraction sensing," Proc. SPIE **6447**, 64470P (2007).
44. M. Galli, S. L. Portalupi, M. Belotti, L. C. Andreani, L. O'Faolain, and T. F. Krauss, "Light scattering and Fano resonances in high-Q photonic crystal nanocavities," Appl. Phys. Lett. **94**(7), 071101 (2009).
45. S. Chakravarty, Y. Zou, W.-C. Lai, and R. T. Chen, "Slow light engineering for high Q high sensitivity photonic crystal microcavity biosensors in silicon," Biosens. Bioelectron. **38**(1), 170–176 (2012).
46. G. Shtenberg, N. Massad-Ivanir, O. Moscovitz, S. Engin, M. Sharon, L. Fruk, and E. Segal, "Picking up the pieces: a generic porous Si biosensor for probing the proteolytic products of enzymes," Anal. Chem. **85**(3), 1951–1956 (2013).
47. D. Threm, Y. Nazirizadeh, and M. Gerken, "Photonic crystal biosensors towards on-chip integration," J. Biophotonics **5**(8–9), 601–616 (2012).
48. M. Huang, A. A. Yanik, T.-Y. Chang, and H. Altug, "Sub-wavelength nanofluidics in photonic crystal sensors," Opt. Express **17**(26), 24224–24233 (2009).

1. Introduction

Optical detection techniques are useful in evaluating different materials without altering the observed objects' structure or characteristics. Biological interactions are one such example, where light can interrogate the biology in a minimally invasive way, without substantially changing the observed analyte or bio-molecular interaction. In many existing biomedical assays the analysis is slow, labor-intensive, and expensive, motivating for the past decade the development of compact assays using micro-fluidics, *e.g.* Lab-on-a-Chip biosensors. The detection is commonly assisted by labels or tags, *e.g.* fluorescent or radioactive materials [1,2]. However, labels can structurally and functionally alter, and interfere with, analyte molecules. Thus, there is a growing interest in optical label-free sensing techniques which rely on local changes in physical parameters such as absorption, scattering or refractive index (RI) [3–5]. In these examples, label-free sensing can be based on localizing or trapping particles or molecules on treated surfaces to change the observed optical properties. Detecting small changes in the RI can be found useful in many applications such as evaluating biochemical molecular interactions [2,6–8], drug detection and drug evaluation [9], medical diagnostics and trace gas detection [10].

Improving detection limit (DL) in RI sensing can be achieved by increasing the quality factor, Q, the spectral sensitivity, S [nm/RIU], or both, since $DL \propto 1/(Q \times S)$ [1]. The DL of many optical sensors is constrained by an intrinsic tradeoff between their spectral sensitivity and quality factor [11]. Typical localized photonic crystal cavities and optical resonators can achieve very high Q values ranging from 10^4 to 10^6 [2], but show a small field overlap with the analyte, and a low detection volume [12], resulting in a low spectral sensitivity and limited usability in medical practice. Moreover, alignment of the incident light beam to the small area of the localized cavities can be challenging [13]. On the other hand, relatively high sensitivity values were reported for surface plasmon resonance (SPR) sensors where the coupling conditions of incident light into surface plasmons are sensitive to small index changes near metal surfaces [14,15]. However, SPR Q values are low due to intrinsic absorption losses in the metals. Such lower Q values in SPR, increase the ambiguity in determining the spectral resonance location in the presence of spectral noise [1]. Therefore, improving Q values for bio-sensors is desirable both in decreasing the detection limit and improving the signal-to-noise ratio. High-Q optical devices are also important in many other applications, such as photonic devices [16,17], quantum electrodynamics [18,19], nonlinear optics [20–22] and light-assisted particle trapping [23–25].

Two-dimensional (2D) photonic crystal slab (PCS) devices are attractive as miniature RI sensors with large sensing areas and are relatively easy to fabricate. The sensing mechanism in such devices is based on detecting the shift of guided resonance (GR) location in the presence of index change of the sensed material overlaid outside the slab. The GRs are of Fano-lineshapes, which can be tuned to much narrower linewidths than pure Lorentzian lineshapes [1,26–28]. Two-dimensional photonic crystal slab GRs can generally be classified into two distinct polarizations: either E_x, $E_y >> E_z$ or H_x, $H_y >> H_z$. The former, in which the

#197981 - $15.00 USD Received 19 Sep 2013; revised 29 Nov 2013; accepted 4 Dec 2013; published 13 Dec 2013

electric field is oriented mainly along the xy plane, is called transverse-electric (TE) like mode. The latter, in which the magnetic field is oriented mainly along the xz plane, is called transverse-magnetic (TM) like mode [29]. Furthermore, special structural designs of PCSs enable access to their 'dark' modes, i.e. modes that lie outside the light-cone. This turns these modes to lower order GRs with higher Q values as compared to the original fundamental modes [26,30]. Coupling to the 'dark GRs', as termed in ref [30], is also associated with symmetry breaking of the conventional homogeneous PCS (HPCS) as demonstrated, for example, in [31,32], and with higher Q values [33–35]. Breaking the HPCS symmetry and accessing higher order modes while obtaining relatively high Q values, ~10^4, with large area PCS lattices was demonstrated by perturbing the HPCS structure [31] or tilting the incident light angle away from normal incidence [36]. It was also shown that altering periodicity either in 2D PCS design [37,38] or in a single cavity structure [39] results in band-folding.

In the present work, we demonstrate experimentally, for the first time, a novel method of lattice geometry-induced coupling to dark modes of a HPCS, using a face-centered 2D crystal pattern, termed the '*checkerboard*' design. By alternating the nano-holes radii in the lattice, we introduce a small perturbation to existing dark modes, which we term 'perturbed dark modes'. These dark modes are '*band-folded*' into the light-cone. These new modes show extraordinary enhancement of Q values as compared to typical GR in a HPCS, and simultaneously improved S values. The combined Q and S enhancements drastically decreases the DL with respect to conventional HPCS microstructures. The paper is organized as follows: in section 2, we present the concept, theoretical background and detailed simulation analysis of the checkerboard design. In section 3, a detailed description of the fabrication process and characterization is provided along with the experimental results and comparison to the theoretical predictions. The theoretical and experimental results are discussed in section 4 and we present the conclusions in section 5.

2. Checkerboard design

The lattice geometries of the HPCS and checkerboard photonic crystal slab (CPCS) are shown in Figs. 1(*a*) and 1(*b*), respectively. For the CPCS design, there are two holes in each unit cell with unequal radii $r_1 \neq r_2$. Enhancement in Q values is achieved due to a higher periodicity order, which provides access to modes that are normally outside the light cone for HPCS and cannot be coupled to external radiation. Figure 1 shows heuristically the concept of CPCS band folding scheme. Macroscopically, photonic crystal slabs support guided modes (GM) of the form $\mathbf{E}_{\mathbf{k},m}(\mathbf{r}) = e^{i\mathbf{k}.\mathbf{r}}\mathbf{U}_{\mathbf{k},m}(\mathbf{r})$, which are propagating 2D Bloch states bounded by the slab. These GM's [Fig. 1(*c*), red dotted line] are characterized by a 2D wave-vector $\mathbf{k} = [k_x, k_y]$ and band index m, which specify the mode frequency, $\omega_{\mathbf{k},m}$, according to the photonic band structure that is shown schematically in Fig. 1(*c*). Some of these modes are '*dark*', that is, they do not couple to the continuum of unbounded radiation as they are located outside the light cone defined by $n\omega < c|\mathbf{k}|$. On the other hand, modes that are inside the light cone $n\omega > c|\mathbf{k}|$ [Fig. 1(*c*), blue dashed line] can couple to the continuum of unbounded radiation, and are known as GRs. Guided resonances in PCS exist due to '*band-folding*' at the Brillouin Zone (BZ) edges. For HPCS, where the nano-holes are identical, the primitive unit cell contains only one hole, and the associated BZ is bounded by $-\pi/a < k_x, k_y < \pi/a$ in the reciprocal k-space.

#197981 - $15.00 USD Received 19 Sep 2013; revised 29 Nov 2013; accepted 4 Dec 2013; published 13 Dec 2013

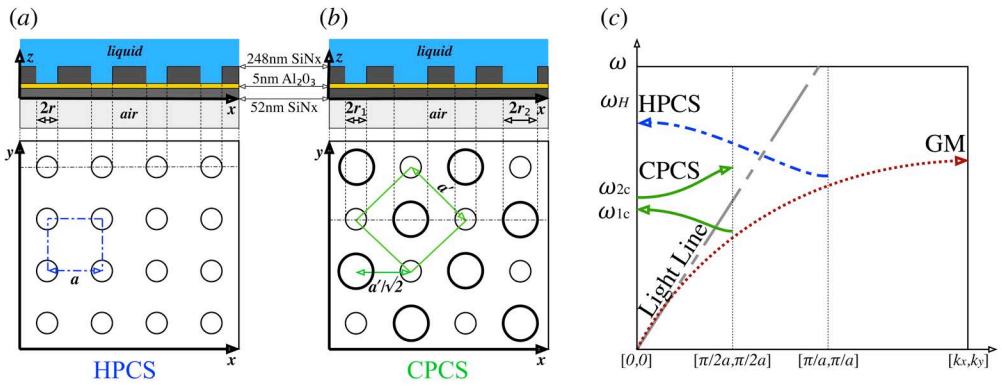

Fig. 1. (Color online). (*a*) Geometry of HPCS reduced unit cell (bounded by the blue dashed line), and (*b*) geometry of CPCS reduced unit cell (bounded by the green solid line), with lattice constant *a*' and the inter-hole distance $a'/\sqrt{2}$. (*c*) Schematic description of CPCS (solid green line), and HPCS (dashed blue line) band-folding starting from a dielectric substrate guided mode (dotted red line) into HPCS GR at $[k_x,k_y] = [\pi/a, \pi/a]$ and into CPCS GR at $[k_x,k_y] = [\pi/2a, \pi/2a]$. In panel (*c*), we have set inter-hole distance of HPCS and CPCS to be the same, resulting in a ratio of $a'/a = \sqrt{2}$ for the lattice constants of CPCS and HPCS. The nano-hole radii are $r_1 = r-\Delta r/2$ and $r_2 = r + \Delta r/2$ for small Δr.

The dark modes (GMs represented by the red dotted line), are folded at $[k_x,k_y] = [\pi/a, \pi/a]$ to the Γ point, namely $[k_x,k_y] = [0, 0]$ and become bright modes or GRs of HPCS (presented in Fig. 1(*a*)), as shown in Fig. 1(*c*) (blue dashed line). In the CPCS design, where radii of adjacent holes are made unequal, $r_1 \neq r_2$ as depicted in Fig. 1(*b*), the primitive unit cell is enlarged to contain two holes. Accordingly, the size of the BZ drastically decreases and additional band folding occurs. More interestingly, the quality factor of these GRs can be tuned to very large values if the difference in nano-hole radii $\Delta r \equiv |r_1-r_2| \to 0$, such that the dielectric structure of CPCS, $\varepsilon^{[C]}(\mathbf{r})$, differs only as a perturbation from the dielectric structure of HPCS $\varepsilon^{[H]}(\mathbf{r})$, *i.e.*, $\varepsilon^{[C]}(\mathbf{r}) = \varepsilon^{[H]}(\mathbf{r}) + \delta\varepsilon(\mathbf{r})$, for $\delta\varepsilon(\mathbf{r})$ being non-zero over a very small portion of volume of the entire unit cell.

The coupling strength of a GM, $\mathbf{E}_{\mathbf{k},m}(\mathbf{r}) = e^{i\mathbf{k}\cdot\mathbf{r}}\mathbf{U}_{\mathbf{k},m}(\mathbf{r})$, that is bounded to the slab and the continuum of unbounded radiation $\mathbf{E}^{\text{ext}}(\omega,\mathbf{r})$ over different ω's, which extends to the far field, is related to the overlap integral defined as [40]:

$$\gamma(\omega) \equiv \int d^3\mathbf{r}\,\varepsilon(\mathbf{r})\left[\mathbf{E}^{ext}(\omega,\mathbf{r})\right]^{*}\mathbf{E}_{\mathbf{k},m}(\mathbf{r}), \qquad (1)$$

where $\mathbf{E}_{\mathbf{k},m}(\mathbf{r})$ and $\mathbf{E}^{\text{ext}}(\omega,\mathbf{r})$ are normalized, and the relative permittivity, $\varepsilon(\mathbf{r})$ describes the dielectric structure, with $\varepsilon = 1$ in vacuum. The overlap integral is non-vanishing only when there is a component in $\mathbf{E}^{\text{ext}}(\omega,\mathbf{r})$ that is phase-matched with the GM. For thin slab, $\gamma(\omega)$ is approximately constant over the relevant frequency range around $\omega_{\mathbf{k},m}$ and we take $\gamma_{\mathbf{k},m} = \gamma(\omega)$. In CPCS $\delta\varepsilon(\mathbf{r})$ occurs over a very small volume, and the coupling of the GM to external radiation is weak. In this weak-coupling limit, $|\gamma_{\mathbf{k},m}|^2$ is approximately proportional to the GM resonance line width, and thus, $|\gamma_{\mathbf{k},m}|^2 \propto 1/Q_{\mathbf{k},m}$, where $Q_{\mathbf{k},m}$ is the quality factor of the $\mathbf{k},m$ GM.

The GM at $[k_x,k_y] = [\pi/a, \pi/a]$ of a HPCS lies outside the light cone and there is no external plane wave component that can satisfy the phase-matching condition, resulting in a dark mode. However, in the CPCS design with $\Delta r > 0$, the GM is folded at $[k_x,k_y] = [\pi/2a, \pi/2a]$ to the Γ point to become bright, and can couple to the incoming plane wave at normal incidence [Fig. 1(*c*), green solid line]. With $\Delta r \to 0$, the coupling strength vanishes, which gives rise to a large quality factor, $Q \to \infty$.

In Figs. 2 and 3, we numerically verify these predictions using the Stanford Stratified Structure Solver (S4), a frequency domain code based on coupled wave analysis and S-matrix

#197981 - $15.00 USD Received 19 Sep 2013; revised 29 Nov 2013; accepted 4 Dec 2013; published 13 Dec 2013

algorithm [41] and a commercial finite-difference time-domain simulation software package: Lumerical FDTD solution from Lumerical Solutions Inc. Making use of the HPCS and CPCS structures detailed in Figs. 1(*a*) and 1(*b*) with equal lattice constant $a_{HPCS} = a'_{CPCS} = 1018$nm (*e.g.* in order to match the resonance wavelength locations), and the following RI values: $n(\text{liquid}) = 1.43$, $n(SiN_x) = 2.02$, and $n(Al_2O_3) = 1.65$, we fit the simulated transmission curves with a Fano line shape [1,26–28] to obtain the Q values of the different TE- and TM- like modes. The Fano line-shape is the result of interference between the GR, which is a discrete mode bounded to the slab, and the continuum of unbounded modes. These unbounded modes are radiations that extend to the far field, with a broad spectral shape associated with the Fabry-Perot spectrum of the slab. This process is repeated for various CPCS designs with different Δr values, and the results are compared to HPCS with different r values.

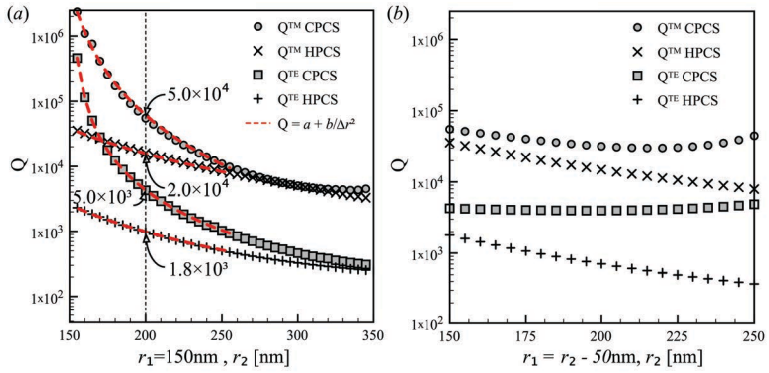

Fig. 2. (Color online) The theoretically predicted CPCS Q values for TE- and TM- like modes as a function of (*a*) increasing nano-hole radius difference in the range of Δr = 5nm to 200nm (fixed r_1 = 150nm, r_2 = 155nm to 350nm) and, (*b*) simultaneously increasing both r_1 and r_2 nano-hole radii, keeping the radius difference fixed at Δr = 50nm. The corresponding HPCS structures of r = 155nm to 350nm and r = 155nm to 250nm are plotted in (*a*) and (*b*), respectively. The lattice constants $a_{HPCS} = a'_{CPCS} = 1018$nm.

According to Fig. 2(*a*), increasing Δr (CPCS), or r (HPCS) will reduce the Q values. The Q values of CPCS are intrinsically higher than those of the HPCS for the tested parameter range. The predicted theoretical Q values for Δr = 50nm (r_1 = 150nm, r_2 = 200nm) are depicted in Fig. 2(*a*) by a vertical black dotted line with $Q^{TM,CPCS} = 5.0 \times 10^4$, $Q^{TE,CPCS} = 5.0 \times 10^3$, $Q^{TM,HPCS} = 2.0 \times 10^4$ and $Q^{TE,HPCS} = 1.8 \times 10^3$, that is, enhancement factors of 2.5 for the TM-like and 2.7 for the TE-like modes, respectively. We see that for CPCS, Q scales as $(1/\Delta r)^2$. According to Eq. (1), for $\Delta r = 0$ the overlap integral vanishes, hence $\gamma(\omega) = 0$. Perturbing the dielectric structure by detuning the nano-holes in Δr causes a step change of the permittivity $\delta\varepsilon$, over a spatial region of volume $V \propto \pi h[(r + \Delta r/2)^2 - (r - \Delta r/2)^2]$, that is, $V \propto \Delta r$. The field pattern remains identical to the dark mode $\mathbf{E}^{\text{dark}}_{\mathbf{k},m}(\mathbf{r})$ of the unperturbed structure, except for local changes at the periphery of the small spatial region. To first order approximation, we can substitute $\mathbf{E}^{\text{dark}}_{\mathbf{k},m}(\mathbf{r})$ for $\mathbf{E}_{\mathbf{k},m}(\mathbf{r})$ in Eq. (1) to obtain $\gamma_{\mathbf{k},m}$, resulting in $Q_{\mathbf{k},m} \propto (1/\Delta r)^2$. This simple relation breaks down only for large values of Δr as shown in Fig. 2(*a*). Figure 2(*b*) further illustrates a relative invariant behaviour for fixed Δr value while increasing both r_1 and r_2. For HPCS, it was found from simulation, shown in Fig. 2, that the quality factor scales as $(1/r)^2$ for the broad range of r values we evaluated. While high Q values can only be obtained in HPCS with small nano-holes, which are challenging to fabricate, in CPCS design, reliable structures with small Δr can be easily fabricated, leading to high Q values.

Next, we examine the sensitivity S [nm/RIU], derived using Eqs. (1) and (2) in ref [42], and is given by,

#197981 - $15.00 USD Received 19 Sep 2013; revised 29 Nov 2013; accepted 4 Dec 2013; published 13 Dec 2013

$$S = \frac{\Delta\lambda_0}{\Delta n} = \lambda_0 \frac{\int_{liquid} d^3\mathbf{r} n(\mathbf{r}) \left|\mathbf{E}_{\mathbf{k},m}(\mathbf{r})\right|^2}{\int_{\infty} d^3\mathbf{r} n^2(\mathbf{r}) \left|\mathbf{E}_{\mathbf{k},m}(\mathbf{r})\right|^2} \tag{2}$$

where λ_0 is the resonance wavelength and $n(\mathbf{r}) = \sqrt{\varepsilon(\mathbf{r})}$ is the RI. Universally, single-mode S is limited by λ_0/n where n is the RI of the sensed substance, considering that all of the mode energy is in the interrogated material [42]. Compared to a conventional HPCS with the same lattice constant, where one hole is considered in a unit cell, S of the CPCS design is enhanced mainly due to two reasons, (*i*) two nano-holes in the single unit cell that yields roughly two fold the detection volume in the hole regions, and (*ii*) the evanescent decay length of the lowest-order CPCS bright mode is larger than the lowest-order bright mode of HPCS, and is thus more sensitive to an index change in the interrogated medium outside the slab. In Fig. 3 we show that the sensitivity of CPCS is intrinsically higher than that of HPCS and the enhancement of sensitivity in enlarging the nano-hole size is more pronounced in CPCS design than in HPCS.

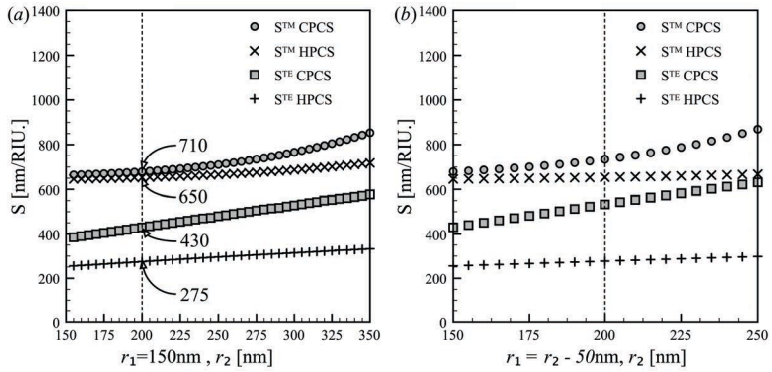

Fig. 3. (Color online) The theoretically predicted S values as a function of (*a*) increasing nano-hole radius difference in the range of Δr = 5nm to 200nm (fixed r_1 = 150nm, r_2 = 155nm to 350nm) and, (*b*) increasing nano-hole radii, where the radius difference is fixed at Δr = 50nm while increasing r_1 and r_2 simultaneously. (see schematic in Fig. 1). The corresponding HPCS structures of r = 155nm to 350nm and r = 155nm to 250nm are plotted in (*a*) and (*b*) respectively. The lattice constants $a_{HPCS} = a'_{CPCS}$ = 1018nm. For all structures, the lattice constants and size of unit cells are the same, but with slightly different peak resonance wavelengths that deviate from around 1550nm for TE-like and 1460nm for TM-like modes.

In the CPCS design, we observe an enhancement of S values with increase of Δr and r [Fig. 3(*a*) and Fig. 3(*b*) respectively]. This effect is weaker for the TM-like mode with respect to the TE-like mode. The sensitivity of CPCS increases with the nano-holes' radii r_1 or r_2 even for fixed Δr as shown in Fig. 3(*b*), while comparatively, the Q values are only slightly altered due to the equivalent change as presented in Fig. 2(*b*). High-Q PCS can be realized in an alternative way by fabricating HPCS with small nano-holes, as shown in Fig. 2(*a*). While theoretically possible, fabrication challenges increase as the hole sizes decrease since a 'perfect' hole is much harder to realize and replicate uniformly over the entire slab in order to achieve a similar Q value. Our proposed CPCS design replaces such stringent fabrication requirement of minimizing hole radius r, with minimizing the difference in radii Δr instead. Each individual hole radius can still be large, which apart from easing the fabrication challenge in obtaining high Q value, also allow larger sensing volume and thus higher sensitivity than HPCS.

Figure 4 shows simulated results of both the horizontal and vertical cross-sections of electric field energy distribution patterns, $\varepsilon(\mathbf{r})|\mathbf{E}(\mathbf{r})|^2$ of various PCS structures with the same

#197981 - $15.00 USD Received 19 Sep 2013; revised 29 Nov 2013; accepted 4 Dec 2013; published 13 Dec 2013

lattice constant. The structures are similar to Figs. 1(*a*), 1(*b*), setting the lattice constants equal namely, $a_{HPCS} = a'_{CPCS} = 1018$nm with modified vertical layer structure as detailed in the figure.

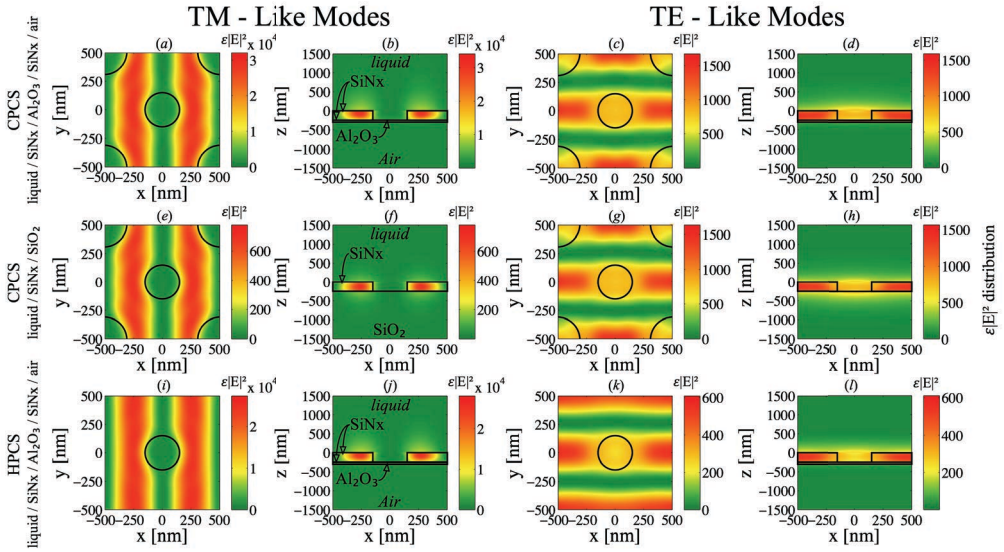

Fig. 4. (Color online) Comparison of the simulated energy distribution patterns, $\varepsilon|(\mathbf{E})|^2$ at *xy*-plane ($z = -124$nm), and *xz*-plane ($y = 0$nm). (*a*-*d*) CPCS TM- and TE- like modes for infinite liquid/258nm SiN_x/5nm Al_2O_3/52nm SiNx/infinite air, (*e*-*h*) CPCS TM- and TE- for infinite liquid/258nm SiN_x/infinite SiO_2 and (*i*-*l*) HPCS TM- and TE- like modes for infinite liquid/258nm SiN_x/5nm Al_2O_3/52nm SiNx/infinite air. Note that the layered structure depicted in the second column (*b*, *f* and *j*) is identical across each row. The simulated refractive index were n(liquid) = 1.43, $n(SiN_x) = 2.02$, $n(Al_2O_3) = 1.65$, and $n(SiO_2) = 1.47$ with exciting wavelength at mode resonance, $\lambda_{TE} \sim 1550$nm and $\lambda_{TM} \sim 1460$nm. The top SiN_x layer was patterned with 150nm and 200nm nano-hole radii.

First, we compare the CPCS to HPCS designs on suspended SiN_x membrane with liquid above and air below as shown in Fig. 4(*a*)-(*d*) and Fig. 4(*i*)-(*l*). We observe an enhancement in the peak field intensities in CPCS over HPCS, by a factor of 4 and 2 for the TE- and TM-like modes respectively (notice the different color bar scales of TE- and TM- like modes on the right of the contour plots). This confirms the superiority of CPCS in enhancing *Q* values over HPCS that is shown in Fig. 2. Secondly, in general, *S* of the TM-like modes is higher than their TE counterparts for both CPCS and HPCS, as a higher proportion of the energy of the TM mode is in the sensed material as shown in Figs. 4(*b*) and (*d*), or Figs. 4(*j*) and (*l*). In comparing the specific TE-like mode *S* of CPCS and HPCS [Figs. 4(*c*) and 4(*k*)], there is an extra hole in the CPCS unit cell with significant electric field, where such hole is absent in the HPCS unit cell. This confirms the larger *S* of the TE-like mode in CPCS over HPCS shown in Fig. 3. For the TM case, such enhancement of *S* due to extra hole in the CPCS unit cell is minimal if the nano-hole radius is small, as the centers of holes lie at the troughs of low energy distribution [Figs. 4(*a*) and (*i*)]. However, further increasing the nano-hole radii beyond the energy trough regions markedly enhances the sensitivity of TM-like mode of CPCS over HPCS, as shown in Fig. 3.

Apart from engineering the photonic crystal mode pattern utilizing the CPCS design, we can further enhance the sensitivity by using a liquid/SiN_x/air structure, with PCS suspended in air, instead of the conventional liquid/SiN_x/SiO_2 structures with a solid SiO_2 cladding. For the TM-like mode, the mode energy in a suspended membrane, as shown in Fig. 4(*b*) can penetrate deeper into the sensed liquid, reaching field intensity values 60 times larger compared to the structure with SiO_2 cladding [Fig. 4(*f*)]. However, a much more modest

#197981 - $15.00 USD Received 19 Sep 2013; revised 29 Nov 2013; accepted 4 Dec 2013; published 13 Dec 2013

enhancement, a factor of 1.5, is observed for the TE-like mode in a suspended membrane, as a significant portion of the mode energy is in the hole region that are inert to the cladding of the slab, as shown by Figs. 4(*d*) and 4(*h*).

3. Sensor fabrications and characterization

3.1 Fabrication of checkerboard photonic crystal lattice on sealed membrane

The CPCS was realized by a unit cell with alternating hole sizes, extending the periodicity of HPCS. Figure 5 shows the top view of a fabricated 2D CPCS obtained using an environmental scanning electron microscope (ESEM), [CNI Quanta 250FEG, Hillsboro, Oregon, USA].

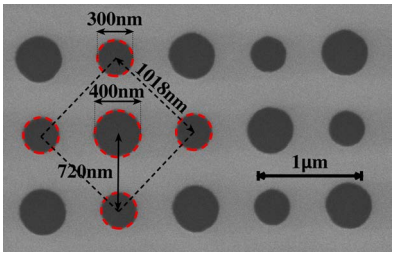

Fig. 5. (Color online) Scanning Electron Micrograph (SEM) image of a checkerboard photonic crystal slab top view [CNI Quanta 250FEG ESEM, beam voltage 10kV] overlaid by a drawing of a unit cell. The lattice constant a_{CPCS} = 1018nm, the nano-holes radii are r_1 = 150nm, r_2 = 200nm respectively with Δr = 50nm. Scale bar is 1μm.

The CPCS nano-structure architecture presented above, can be implemented in several vertical device architectures including liquid/SiN_x/SiO_2, and a suspended membrane of liquid/SiN_x/liquid [28]. Figure 6 shows the schematic representation of the fabricated vertical layer stack. The SiN_x layers were deposited by low-pressure chemical vapor deposition (LPCVD) technique, while the Al_2O_3 layer was deposited by an atomic layer deposition (ALD) technique. The substrate was selectively removed in some locations to create air/SiN_x/liquid vertical device architecture [Figs. 6(*a*) and 6(*b*)]. Two sets of holes were etched in the top SiN_x layer [Fig. 6(*c*)].

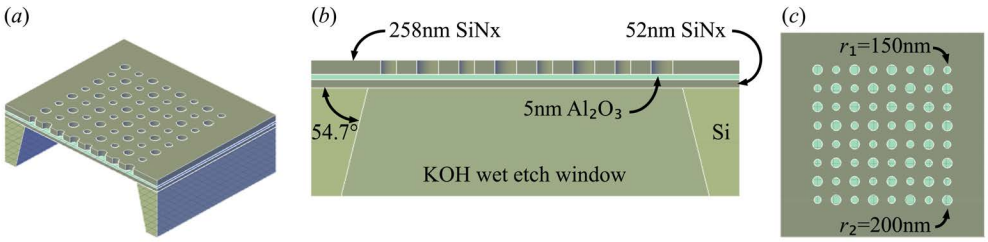

Fig. 6. (Color online) Schematics of the liquid/SiN_x/air suspended membrane design. (a) 3D view of the layers structure and window after KOH wet etch removal of the Si substrate, (b) layer structure cross-section and, (c) top view demonstrating the fabricated CPCS nano-hole array.

Reactive Ion Etching (RIE) is used to transfer the CPCS pattern into the top SiN_x layer in the suspended membrane design [43]. The 5nm Al_2O_3 layer acts as an etch stop layer which improves hole etching, resulting in better vertical uniformity for the nano-holes. The PCS patterned mesa size was limited to 300μm in diameter in order to avoid pattern *stitching* during e-beam lithography [Vistec EBPG 5000 + e-beam lithographer, 5nm resolution] as shown in Fig. 5.

#197981 - $15.00 USD Received 19 Sep 2013; revised 29 Nov 2013; accepted 4 Dec 2013; published 13 Dec 2013

3.2 Quality factor characterization of checkerboard photonic crystal

Quality factors, Q, were characterized numerically and experimentally for the CPCS design presented in Figs. 1, 5 and 6. The schematic representation of the experimental optical system used to characterize Q and S values for the PCS devices is presented in Fig. 7. During the measurement we used either water or RI calibrated liquids [Cargille Labs, Cedar Grove, NJ, USA], placed above the sensor surface. A thin cover glass was used to seal the sample and minimize evaporation from the top patterned surface. A Supercontinuum broadband laser light source [650 – 1700 nm, 200 mW, MicroLase, Fianium] was used and the beam was collimated, polarized and focused onto the CPCS patterned mesa area. The transmitted light was crossed-polarized in 90° with respect to the incident beam and was then collected into a single-mode fiber connected to an optical spectrum analyzer (OSA). This crossed-polarized measurement technique enabled us to reduce the unwanted Fabry-Perot fringes that were introduced by the cover glass. The measured CPCS device was mounted on both a translation (xyz) stage and a rotation stage enabling the required degrees of freedom for characterization.

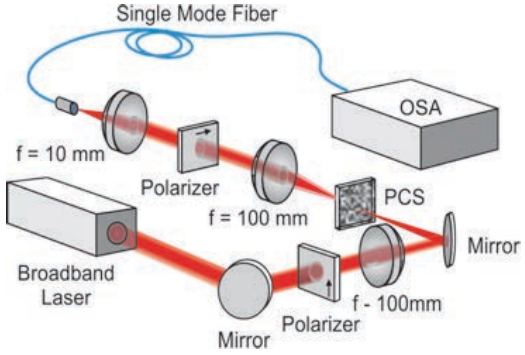

Fig. 7. (Color online) Experimental setup used for characterizing the CPCS and HPCS devices.

The experimental results were compared to numerical predictions using the Stanford Stratified Structure Solver (S4) and Lumerical FDTD solution. Both CPCS TE-like and TM-like fundamental modes (lower frequencies than HPCS), and other higher order modes were analyzed. Figure 8 shows S4 simulation results for the band-diagram and the corresponding spectral transmission curve of normal incidence plane wave at the Γ point. This analysis enables specific identification of the CPCS modes that are later measured in experiments and presents a broad understanding of the mode structure for the CPCS design. The transmission curve (solid red line) was obtained for a normal-incidence plane wave. Field patterns are plotted for the different resonances obtained at normal-incidence. The band-diagram data points (Fig. 8(*a*), right) were obtained by simulating the transmission curves for different incident angles, fitting the resonances using a Fano line-shape and retrieving the resonance wavelength, which yields the dispersion curves' data points. The dark modes were identified by a characteristic disappearance of the mode resonance at normal incident angle. Excitation of both TE- and TM- like modes is possible due to existence of all fields' components for all the investigated modes in 2D PCS geometry. We note that for off-normal incidence, there is no clear distinction between TE- and TM- like modes and the mode patterns should be carefully evaluated.

#197981 - $15.00 USD Received 19 Sep 2013; revised 29 Nov 2013; accepted 4 Dec 2013; published 13 Dec 2013

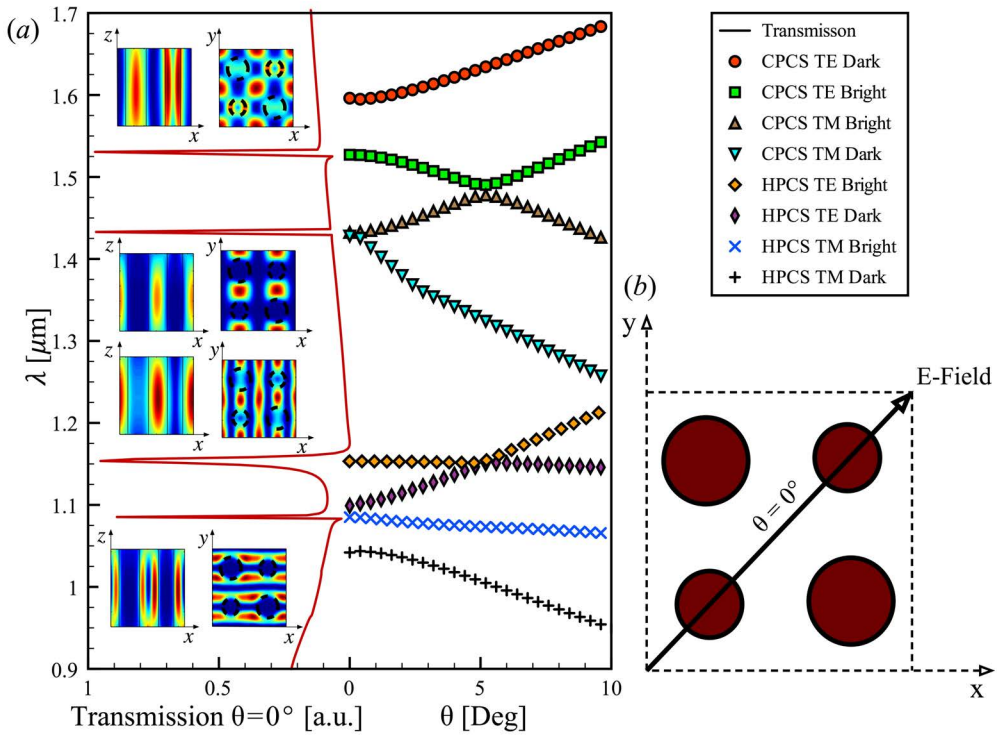

Fig. 8. (Color online) (*a*) P-polarization band diagram with incident E-field polarization at 45°, and the corresponding CPCS transmission spectrum at normal incidence (red solid line). In the insets are the electric field energy profile $\varepsilon|(\mathbf{E})|^2$ for the different simulated modes. "TE/TM", "Bright/Dark" are labeled according to the mode at θ=0°. (*b*) Definition of Electric field polarization with respect to CPCS lattice. The xy-planes are at z = 0 and xz-planes are at y = 0.25*a*.

In this simulation, the periodicity, hole radius and wafer design are similar to those presented in Fig. 5. The liquid layer above and underlying air layer below the slab were extended to infinity to simplify the simulation and ensure numerical convergence. The liquid/SiN_x/air device included a patterned 258nm thick SiN_x membrane on top of a 52nm thick SiN_x un-patterned layer similar to that presented in Fig. 6.

Our simulation predicts that the Q values of fundamental CPCS modes at λ_{TE} = 1.53μm and λ_{TM} = 1.43μm are $Q_{TE} = 4.5 \times 10^3$ and $Q_{TM} = 5.0 \times 10^4$, respectively. These are higher than the Q values of the HPCS modes that are found at λ_{TE} = 1.15μm and λ_{TM} = 1.08μm, with $Q_{TE} = 1.8 \times 10^3$ and $Q_{TM} = 2.0 \times 10^4$, respectively. The $\varepsilon(\mathbf{r})|\mathbf{E}(\mathbf{r})|^2$ patterns (Fig. 4 and see insets of Fig. 8), support the suggested increase in Q values, when comparing the CPCS and HPCS mode profiles. Larger energy confinements in the hole regions for the TE-like mode and in the dielectric regions of the slab for the TM-like mode are observed for the CPCS structures, as compared to the corresponding HPCS structures, similar to that in Fig. 4. We crosschecked the results using different simulation techniques: transfer matrix and FDTD, and obtained almost identical resonance spectral locations to within 1nm resolution, and the Q values matched to within 1%.

Next, we fabricated and experimentally characterized the proposed CPCS and the corresponding HPCS structures. Figure 9 shows a comparison between the measured TE- and TM-like resonances for the CPCS and HPCS structures, the fitted Q, and the Q value for each resonance peak.

#197981 - $15.00 USD Received 19 Sep 2013; revised 29 Nov 2013; accepted 4 Dec 2013; published 13 Dec 2013

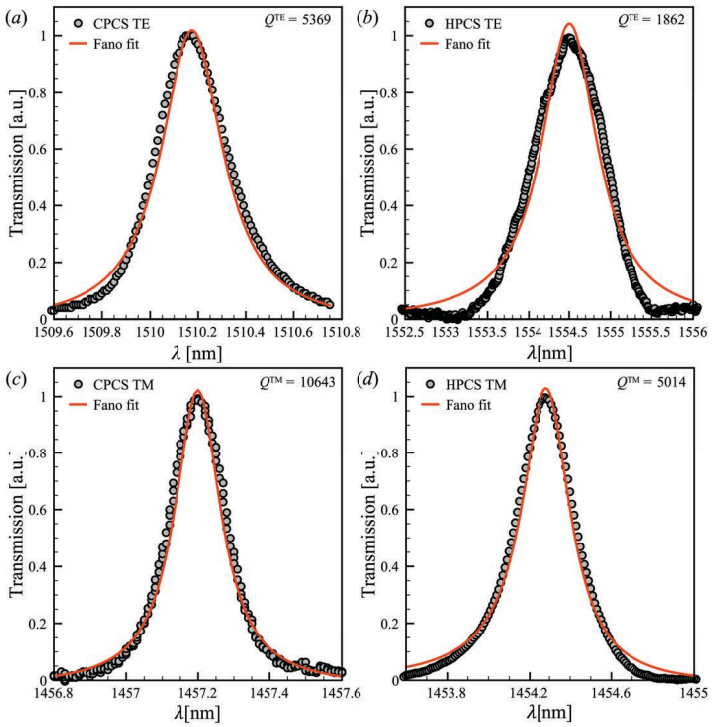

Fig. 9. (Color online) Quality factor, Q analysis using normal incident cross-polarized light in transmission mode, comparing CPCS (r_1 = 150nm, r_2 = 200nm) vs. HPCS (r = 150nm) TE and TM like modes for liquid RI, n = 1.43 and layered structure of liquid, 258nm thick SiN_x, 5nm thick Al_2O_3, 52nm thick SiN_x and air. (*a*) CPCS TE-like experimental waveform, (*b*) HPCS TE-like experimental waveform, (*c*) CPCS TM-like experimental waveform and, (d) HPCS TM-like experimental waveform.

A Fano line-shape was fitted to the measured data in order to obtain the Q values [26,44]. We observe that the line-shape is close to a Lorentzian profile, indicating that the crossed-polarized measurement technique indeed significantly suppress the unwanted Fabry-Perot effects in the measured spectral waveforms. The observed Q values for the CPCS are Q_{TE} = 5369 and Q_{TM} = 10643 [Fig. 9(*a*) and 9(*c*) respectively], which are higher, as predicted by theory, than those of HPCS, Q_{TE} = 1863 and Q_{TM} = 5014 [Fig. 9(*b*) and 9(*d*) respectively]. The simulation for the TE-like GR modes agrees well with measured Q value data (< 7% for CPCS and < 4% for HPCS), while a disagreement exists between the measured and simulated Q values for TM-like GR. It is well known that TM modes, with their much higher Q values in ideal situations, are more sensitive to fabrication tolerances, surface roughness and absorption losses [36].

3.3 Sensitivity characterization of checkerboard photonic crystal

We have measured the bulk sensitivity, $S[\text{nm/RIU}]$ of our CPCS design by placing different values of RI liquids [Cargille Labs, Cedar Grove, NJ, USA] above the top patterned surface, covering the top surface and penetrating the holes in the device, while observing the resulting spectral resonance shifts as shown in Fig. 10, for the CPCS suspended membrane (liquid/SiN_x/air) structure. These experimental spectral shifts were compared to the simulated values presented in Fig. 3. A similar analysis was conducted for HPCS as well. The shift in the resonance wavelength due to application of different RI liquids is translated into spectral sensitivity in Fig. 10(*c*), by fitting a regression line to the experimental data.

#197981 - $15.00 USD Received 19 Sep 2013; revised 29 Nov 2013; accepted 4 Dec 2013; published 13 Dec 2013

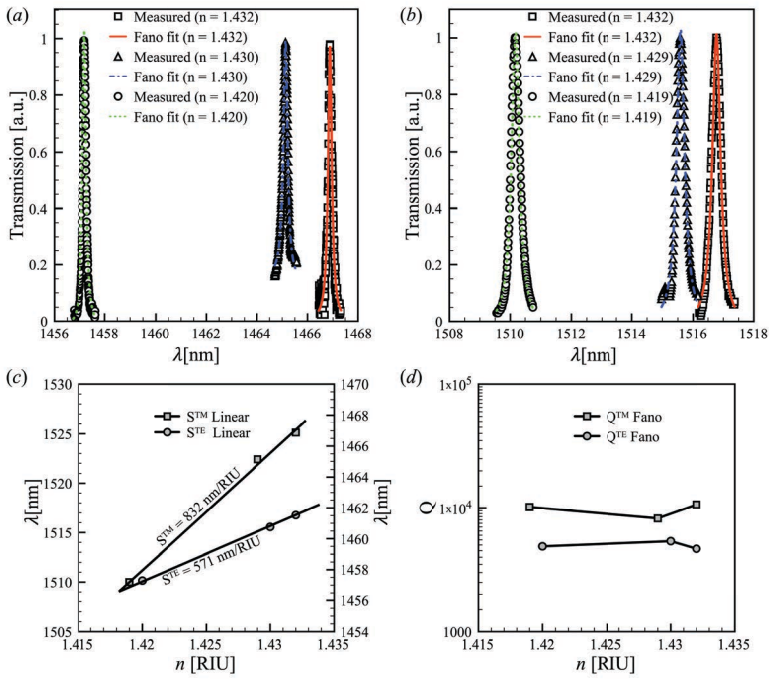

Fig. 10. (Color online) Sensitivity evaluation of CPCS TM and TE like GR modes with same parameters as in Fig. 9. (*a*) Measured TM-like experimental spectral waveforms for 3 different RI's (*b*) TE-like experimental spectral waveforms for 3 different RI's (*c*) Fitted experimental TM- and TE-like sensitivity values and, (*d*) experimental TM- and TE-like quality factors.

The resulting *S* values for a similar suspended membrane design, liquid/SiN_x/air, for both CPCS and HPCS are presented in Table 1 and compared to the theory.

Table 1. Comparison between experimental and theoretical sensitivity values

S	Experimental		S4		Theoretical limit
	CPCS	HPCS	CPCS	HPCS	n = 1.43
	r_1 = 150nm	r = 150nm	r_1 = 150nm	r = 150nm	
	r_2 = 200nm		r_2 = 200nm		
S_{TM}[nm/RIU]	832	707	710	650	1018
S_{TE}[nm/RIU]	571	310	430	275	1055

The results demonstrate a discrepancy of 25% for TE- and 15% for TM- like modes in the CPCS and 9% for TE- and 12% for TM- like modes in the HPCS.

4. Discussion

In this work we designed, fabricated and characterized a novel CPCS with superior sensitivity, S_{TM} = 832nm/RIU, and higher quality factor, Q_{TM} = 10643, than regular HPCS in a relatively small mesa size ≤300μm × 300μm. These results present an increase in *Q* values by a factor >2 for TM- and >2.5 for TE-like modes in CPCS design with respect to HPCS. The sensitivity, *S* is enhanced by a factor of >1.2 for TM-like and >1.8 for TE-like modes in the CPCS geometry. These exciting results are novel in circumventing the theoretical constraints of *Q* and *S* trade-offs in conventional PCS structures [28,45]. Making use of this new geometry allows us to realize high-*Q* PCS structures with relatively large nano-holes (as an example, a CPCS with r_1 = 150nm and r_2 = 200nm) resulting in easier device fabrication. The high-*Q* values are attributed to coupling to previously dark GMs of HPCS, which due to CPCS lattice geometry, are band-folded to become bright. The enhanced *S* values are the

#197981 - $15.00 USD Received 19 Sep 2013; revised 29 Nov 2013; accepted 4 Dec 2013; published 13 Dec 2013

result of increased nano-hole sizes, optimized vertical layer architecture, and lower-order modes resulting in enhancement of the energy distribution in the interrogated material as demonstrated in Fig. 4.

The energy distributions depicted in Fig. 4 and in the insets of Fig. 8 highlight the superiority of CPCS design over the HPCS design for both TE- and TM-like modes. CPCS TE-like mode energy is twice that of the HPCS, while the CPCS TM-like mode intensity is increased in the sensed material by a factor of 4. Moreover, suspending the SiN_x showed major improvement in the TM-like mode energy distribution over that of liquid/SiN_x/SiO_2 layer structure. These findings are particularly interesting considering a possible application such as analyzing the presence of analyte inside or outside the nano-holes [46]. The underlying intact (un-patterned) 52nm SiN_x layer helps in sealing the PCS device and in preventing the sensed liquid from leaking to the underlying air region. Additionally, removal of the Si substrate eliminates most of the parasitic Fabry-Perot effects.

The predicted spectral picture for transmission intensity and band-diagram plots in Fig. 8 reveals a rich hierarchy of mode patterns. Comparing the HPCS to the CPCS fundamental modes, the CPCS mode is lower in frequency and thus, penetrates deeper into the sensing material [26,31]. Following Fig. 2 and Fig. 9, it is demonstrated that the CPCS fundamental mode has intrinsically higher Q thus, making use of the reasoning in Fig. 8, we predict high-Q values even for relatively large off-normal incident angles.

Quality factors in CPCS designs as high as Q_{TM} = 10643 for the TM-like, and Q_{TE} = 5369 for the TE-like GR modes were experimentally measured for normal-incidence crossed-polarized beam. The simulated and measured Q_{TE} values agree well to within 7% and 5% for CPCS and HPCS respectively [see Figs. 2, 3, 9 and 10]. Simulated Q_{TM} values are higher than those obtained experimentally. The TM-like modes are far more prone to various imperfections in fabrication and experimental procedures that degrade the Q-values from the ideal situations of perfect plane waves incident on an infinite mesa, which were assumed in the simulations. In reality, the incident beam has a Gaussian profile with a spot size (the beam diameter at $1/e^2$ intensity points) of ~70μm at the sample that gives rise to non-vanishing lateral wave vectors. Propagation of these off-normal wave components in the lateral direction and the scattering at the boundaries of a finite-sized mesa severely limits the modal lifetime and the highest achievable Q_{TM} values in experiments.

The experimental values of S_{TE} and S_{TM} for the CPCS design are increased by a factor of >1.2 and >1.8, respectively, relative to the corresponding S values of HPCS. The theoretically predicted S values [Fig. 3] are lower than those measured in the experiments as depicted in Table 1. Simulating the sensitivity with high accuracy is challenging due to many uncertainties involved in establishing the design parameters, such as the exact RI values of the different layers and liquids, surface roughness, hole etching angle, *etc.*, as these all translate into ambiguity in simulated S values. The implementation in a SiN_x air-suspended membrane contributed to the enhancement in S as presented in Fig. 4 by re-distributing the mode energy into the sensed material. Moreover, the added extra nano-hole in the CPCS unit-cell increased the sensed volume [see Fig. 2 and Fig. 3].

The single-mode theoretical upper limit of S is given by $S \leq \lambda_0/n$, where λ_0 is the mode resonance wavelength and n is the RI of the sensed material [42]. We experimentally demonstrated S values that are 50% for the TE-like and 80% for the TM-like modes of the theoretically predicted maximal sensitivity [see Table. 1]. These results are significantly improved over previous reported values of up to ≤600nm/RIU [47] and ref. therein. These important findings demonstrate that one can design 2D PCS RI sensor and shape the fields to penetrate deeper into the sensed material, to greatly improve S in detecting small RI changes. High sensitivity values can be realized in a HPCS structure using relatively large nano-holes [48]. This leads to reduced Q values < 1000, which is related to the Q-S trade-off. In this work the checkerboard design, shows simultaneously high Q > 5000 and S > 500, as was demonstrated both theoretically (see Figs. 2 and 3) and experimentally (Figs. 9 and 10).

#197981 - $15.00 USD Received 19 Sep 2013; revised 29 Nov 2013; accepted 4 Dec 2013; published 13 Dec 2013

As photonic crystals have been reported to have a Q and S values trade-off [28,45] that constrains the $DL \propto \kappa\lambda_0/(Q \cdot S)$, our new CPCS lattice design can overcome this trade-off to radically lower the DL. Such improvement is attributed to the fact that very large holes can be used to obtain high S values, without degrading the Q values as compared to conventional PCSs. The quality factor can be independently tuned by decreasing the difference in hole radii $|r_1 - r_2|$ to obtain a GR mode pattern that is perturbed slightly from the dark mode supported by the unperturbed dielectric structure of higher-symmetry [31], the HPCS in our case.

Spectral noise, which arises from temperature fluctuations, laser instabilities, shot noise in photo-detectors, *etc*, can compromise the detection limit by broadening and deforming the resonance lineshape from pure Lorentzian. Our realization of high-Q PCS sensors can filter out a large amount of spectral noise to improve the signal-to-noise ratio, thus protect the achieved detection limit from noise degradation. With such high-Q structures, experiments are required to be performed in the limit of long measurement time [1]. In this limit, $\kappa\lambda_0 \rightarrow 1$ and using $DL \propto \kappa\lambda_0/(Q \cdot S)$, the achievable detection limits for the CPCS design are $DL_{TM} = 1.6 \times 10^{-7}$ RIU and $DL_{TE} = 4.9 \times 10^{-7}$ RIU. The theoretical prediction for the *single mode* detection limit is $DL_{TM} = 2.8 \times 10^{-8}$ RIU and $DL_{TE} = 2.8 \times 10^{-7}$ RIU. We observe that the TE detection limit is in good agreement with the prediction. The relatively low experimental Q_{TM} values with respect to theory contribute to the discrepancy in DL_{TM}. Overall, these Q and S values are, to the best of our knowledge, the highest reported yet for 2D PCS RI sensors.

5. Summary and conclusions

We present a novel technique of coupling light to slightly perturbed dark modes that improves the detection limit of 2D photonic crystal slab based refractive index sensors by an order of magnitude with respect to existing photonic crystal slab structures. Furthermore, the proposed new design reduces fabrication complexity by removing the constraint of small nano-structure sizes for high-Q devices. This new scheme lays the ground for high-precision miniature refractive index sensors with simplified structures.

Acknowledgements

The authors are grateful for the helpful discussions with Shanhui Fan and Victor Liu, Center for Nanoscale Science and Engineering, Stanford University, Stanford, CA and Iliya Sigal, University of Toronto. This work was supported in part through the University of Toronto departmental start-up funds to OL, the Natural Sciences and Engineering Research Council of Canada (NSERC) Discovery Grant RGPIN-355623-08, Collaborative Health Research Project Grant CPG-121050 and by the Networks of Centres of Excellence of Canada, Canadian Institute for Photonic Innovations (CIPI). RG acknowledge partial support through MITACS postdoctoral fellowship; CN and RS acknowledge support through NSERC CREATE Match graduate fellowships; WTL acknowledge the support through the Croucher Foundation Fellowship of Hong Kong.

#197981 - $15.00 USD Received 19 Sep 2013; revised 29 Nov 2013; accepted 4 Dec 2013; published 13 Dec 2013